Article

Limits on Variations in Protein Backbone Dynamics from Precise Measurements of Scalar Couplings

Beat Vgeli, Jinfa Ying, Alexander Grishaev, and Ad Bax

J. Am. Chem. Soc., **2007**, 129 (30), 9377-9385• DOI: 10.1021/ja070324o • Publication Date (Web): 04 July 2007

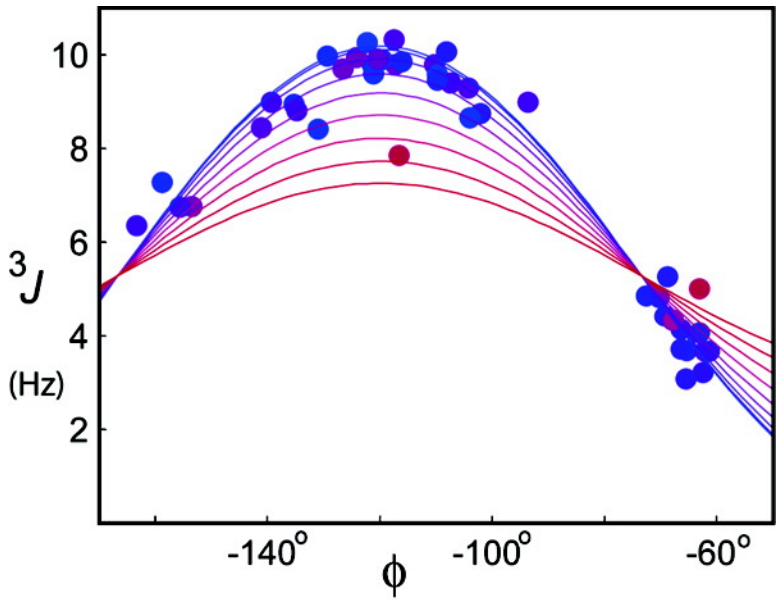

More About This Article

Additional resources and features associated with this article are available within the HTML version:

- Supporting Information
- Links to the 3 articles that cite this article, as of the time of this article download
- Access to high resolution figures
- Links to articles and content related to this article
- Copyright permission to reproduce figures and/or text from this article

View the Full Text HTML

J|A|C|S
ARTICLES
Published on Web 07/04/2007

Limits on Variations in Protein Backbone Dynamics from Precise Measurements of Scalar Couplings

Beat Vögeli, Jinfa Ying, Alexander Grishaev, and Ad Bax*

Contribution from the Laboratory of Chemical Physics, National Institute of Diabetes and Digestive and Kidney Diseases, National Institutes of Health, Bethesda, Maryland 20892

Received January 16, 2007; E-mail: bax@nih.gov

Abstract: $^3J_{H^N,H^\alpha}$, $^3J_{H^N,C^\beta}$, and $^3J_{H^N,C'}$ couplings, all related to the backbone torsion angle ϕ, were measured for the third immunoglobulin binding domain of protein G, or GB3. Measurements were carried out using both previously published methods and novel sequences based on the multiple-quantum principle, which limit attenuation of experimental couplings caused by finite lifetimes of the spin states of passive spins. High reproducibility between the multiple-quantum and conventional approaches confirms the accuracy of the measurements. With few exceptions, close agreement between $^3J_{H^N,H^\alpha}$, $^3J_{H^N,C^\beta}$, and $^3J_{H^N,C'}$ and values predicted by their respective Karplus equations is observed. For the three types of couplings, up to 20% better agreement is obtained when fitting the experimental couplings to a dynamic ensemble NMR structure, which has a ϕ angle root-mean-square spread of $9 \pm 4°$ and was previously calculated on the basis of a very extensive set of residual dipolar couplings, than for any single static NMR structure. Fits of ^3J couplings to a 1.1-Å X-ray structure, with hydrogens added in idealized positions, are 40−90% worse. Approximately half of the improvement when fitting to the NMR structures relates to the amide proton deviating from its idealized, in-peptide-plane position, indicating that the positioning of hydrogens relative to the backbone atoms is one of the factors limiting the accuracy at which the backbone torsion angle ϕ can be extracted from ^3J couplings. Introducing an additional, residue-specific variable for the amplitude of ϕ angle fluctuations does not yield a statistically significant improvement when fitting to a set of dynamic Karplus curves, pointing to a homogeneous behavior of these amplitudes.

Introduction

Intramolecular backbone motions in proteins have been extensively studied by measurement of the backbone amide ^{15}N T_1 and T_2 relaxation times and the heteronuclear $^{15}N-\{^1H\}$ nuclear Overhauser effect.[1−5] However, only the amplitude of dynamics taking place on a time scale faster than the overall rotational correlation time can be quantitatively characterized from such measurements.[6] Considering that many biologically relevant processes are associated with internal motions taking place on much slower time scales, approaches that can define these slower dynamics are of great interest. Two quite different types of experiments potentially provide access to characterization of such processes: measurement of exchange contributions to the transverse relaxation rates, resulting from the change in chemical shift associated with a change in conformation, and measurement of residual dipolar couplings (RDCs). Quantitative measurement of the exchange contribution, commonly carried out by relaxation-dispersion-type measurements, can accurately define the time scale on which the internal motions take place, but can identify motional amplitudes only in special cases.[4,7] Measurement of residual dipolar couplings integrates the orientation of corresponding bond vectors relative to the molecular alignment tensor over a time scale of milliseconds, and therefore intrinsically contains information about both fast and slow internal motions, but not about their temporal behavior.[8−11] In this respect, it is important to note that multiconformer ensembles of NMR structures provide small but statistically significant cross-validated improvements with experimental RDCs over the use of a single conformer.[12−16] Analysis of a large number of RDCs, measured for the small protein GB3, in terms of slow correlated backbone motions also yielded improved agreement with previously measured J

(1) Dellwo, M. J.; Wand, A. J. *J. Am. Chem. Soc.* **1989**, *111*, 4571−4578.
(2) Kay, L. E.; Torchia, D. A.; Bax, A. *Biochemistry* **1989**, *28*, 8972−8979.
(3) Peng, J. W.; Wagner, G. *J. Magn. Reson.* **1992**, *98*, 308−332.
(4) Palmer, A. G. *Chem. Rev.* **2004**, *104*, 3623−3640.
(5) Boehr, D. D.; Dyson, H. J.; Wright, P. E. *Chem. Rev.* **2006**, *106*, 3055−3079.
(6) Lipari, G.; Szabo, A. *J. Am. Chem. Soc.* **1982**, *104*, 4546−4559.
(7) Eisenmesser, E. Z.; Millet, O.; Labeikovsky, W.; Korzhnev, D. M.; Wolf-Watz, M.; Bosco, D. A.; Skalicky, J. J.; Kay, L. E.; Kern, D. *Nature* **2005**, *438*, 117−121.
(8) Tolman, J. R.; Flanagan, J. M.; Kennedy, M. A.; Prestegard, J. H. *Nat. Struct. Biol.* **1997**, *4*, 292−297.
(9) Meiler, J.; Prompers, J. J.; Peti, W.; Griesinger, C.; Bruschweiler, R. *J. Am. Chem. Soc.* **2001**, *123*, 6098−6107.
(10) Peti, W.; Meiler, J.; Bruschweiler, R.; Griesinger, C. *J. Am. Chem. Soc.* **2002**, *124*, 5822−5833.
(11) Tolman, J. R. *J. Am. Chem. Soc.* **2002**, *124*, 12020−12030.
(12) Ottiger, M.; Delaglio, F.; Marquardt, J. L.; Tjandra, N.; Bax, A. *J. Magn. Reson.* **1998**, *134*, 365−369.
(13) Clore, G. M.; Schwieters, C. D. *J. Am. Chem. Soc.* **2004**, *126*, 2923−2938.
(14) Bernado, P.; Blackledge, M. *J. Am. Chem. Soc.* **2004**, *126*, 4907−4920.
(15) Lindorff-Larsen, K.; Best, R. B.; DePristo, M. A.; Dobson, C. M.; Vendruscolo, M. *Nature* **2005**, *433*, 128−132.
(16) Clore, G. M.; Schwieters, C. D. *J. Mol. Biol.* **2006**, *355*, 879−886.

10.1021/ja070324o

couplings through backbone−backbone hydrogen bonds.[17] Variations in local backbone dynamics from the RDC measurements often are found to be remarkably large and depend on the type of analysis employed. For example, considerable differences are observed between backbone dynamics derived for ubiquitin from overlapping sets of RDCs when using two different approaches to interpret these data.[10,13,18] However, in all cases, the amplitudes of backbone dynamics integrated over the entire submillisecond time scale are found to be larger than corresponding amplitudes derived from relaxation measurements. Experimental ^3J couplings represent the population-weighted averages of the instantaneous couplings over a time scale of milliseconds[19−21] and therefore provide an alternate way to evaluate the amplitude of dynamics taking place on a time scale from femto- to milliseconds.[22,23] For example, for a residue in an extended backbone segment, with $\langle\phi\rangle \approx -120°$, large ϕ angle fluctuations decrease $^3J_{H^N,H^\alpha}$ significantly relative to the value expected for the averaged ϕ angle.[21] A previous comparison of experimental ^3J couplings related to peptide backbone angles ϕ in ubiquitin with values expected on the basis of density functional theory (DFT) calculations suggested rather large root-mean-square (rms) fluctuations of 24°, but with this rms value being rather sensitive to the level of theory at which the DFT calculations were carried out.[22]

Here, we evaluate whether three-bond J couplings support the large variation in backbone dynamics concluded from RDC analysis. Our study is carried out for GB3, in part because a very large set of RDCs already has been reported for this protein domain, resulting in a very precise structure, and also because it has been the subject of various modes of analysis, in particular concerning its dynamics in aqueous solution. Moreover, the small size and high solubility of GB3 permit its backbone-related J couplings to be measured at high precision.

In principle, six different three-bond J couplings report on the backbone angle ϕ: $^3J_{H^N,H^\alpha}$, $^3J_{H^N,C^\beta}$, and $^3J_{H^N,C'}$, as well as $^3J_{C',H^\alpha}$, $^3J_{C',C^\beta}$, and $^3J_{C',C'}$. A variety of experiments for the measurement of these couplings have been proposed over the years,[24−28] and results reported for ubiquitin indicated their values to be highly self-consistent as well as being in good agreement with a single static X-ray structure.[29,30] However, measurement of such couplings is affected by the finite lifetime of the passive spin (J-coupled to the spin observed directly), decreasing the measured splitting by an amount that depends both on the size of the J splitting itself and on the selective T_1 value of the passive spin.[31] An elegant solution to this complication has been put forward by Rexroth et al.,[32] who proposed to measure the $^3J_{H^N,H^\alpha}$ value from the difference of two much larger, multiple-quantum (MQ) J splittings, which each are much less affected by the finite lifetime effect.[32] Here, we extend the same concept to measurement of $^3J_{H^N,C^\beta}$ and $^3J_{H^N,C'}$ and compare results with those obtained using conventional, E.COSY-based[25,33] techniques. Results show very close agreement between these two different modes of measurement, and thereby exclude the possibility of substantial systematic errors in the data.

In past parametrizations of Karplus curves for ^3J couplings observed in proteins, dihedral angles always have been derived from X-ray structures, with hydrogens added to these structures under the assumptions of ideal tetrahedral geometry at C^α and idealized, in-plane positions of H^N. For GB3, a very high-resolution X-ray structure is available, as well as multiple NMR structures based on a very large number of RDCs, measured in five different media.[16,17,34] The $C'-N-C^\alpha-C'$ backbone torsion angles, ϕ, in the NMR[34] and X-ray[35] structures are quite close (pairwise rmsd of 3.4°). However, while for the X-ray structure coordinates for the lacking hydrogen atoms were added assuming idealized covalent geometries, in the NMR structure the experimentally determined ^{1}H positions deviate from idealized positions. As a result, the differences in dihedral angles involving protons in the X-ray and NMR structures, e.g., $H^N-N-C^\alpha-H^\alpha$, are nearly twice that value (rmsd 6.5°). A second goal of our study, therefore, is to evaluate whether ^3J couplings follow these distortions from ideality or track the torsion angle defined by the C and N atoms.

Experimental Section

Sample Preparation. The protein GB3 was expressed and purified as described previously.[34] The {^{13}C,^{15}N}-labeled and {^{2}H,^{13}C,^{15}N}-labeled NMR samples contained 350 μL of 4 mM and 500 μL of 2 mM protein solution, respectively, in 95% H_2O, 5% D_2O, 50 mM potassium phosphate buffer, pH 6.5, and 0.5 mg/mL sodium azide.

NMR Spectroscopy. All experiments were performed on a Bruker DMX 600 MHz spectrometer, equipped with a three-axis gradient triple-resonance probe, operating at 298 K. All measurements of $^3J_{H^N,H^\alpha}$ were carried out using the protonated sample. All measurements of $^3J_{H^N,C'}$ and $^3J_{H^N,C^\beta}$ were performed using {^{2}H,^{13}C,^{15}N}-labeled GB3.

The 3D CT-MQ($^1H^N$,$^{13}C^\alpha$)+SQ($^1H^N$)-HNCA spectra (CT = constant-time, SQ = single quantum) for $^3J_{H^N,H^\alpha}$ measurements (Figure 1a) were recorded with 76 (t_1) × 32 (t_2) × 1024 (t_3) complex points, κ values of 1 and 2, t_{1max} = 25.8 ms, t_{2max} = 19.2 ms, t_{3max} = 122 ms, an interscan delay of 0.8 s, and 16 scans per free induction decay (FID). The 3D CT-MQ($^1H^N$,$^{13}C^\alpha$)-HNCA spectrum for the $^3J_{H^N,C'}$ measurement was recorded with the scheme of Figure 1b, using 144 (t_1) × 32 (t_2) × 1024 (t_3) complex points, t_{1max} = 49.0 ms, t_{2max} = 19.2 ms, t_{3max} = 122 ms, an interscan delay of 0.8 s, and 8 scans per FID. The 3D MQ-($^1H^N$,$^{13}C^\alpha$)-HNCA spectra for $^3J_{H^N,C^\beta}$ measurements (Figure 1c) were recorded using 256 (t_1) × 32 (t_2) × 1024 (t_3) complex points, t_{1max} = 87 ms, t_{2max} = 19.2 ms, t_{3max} = 122 ms, an interscan delay of 0.7 s, and 4 scans per FID. The time domain data of all experiments were apodized with a 90°-shifted squared sine bell function in the t_1 dimension and 90°-shifted sine bell functions in the t_2 and t_3 dimensions,

(17) Bouvignies, G.; Bernado, P.; Meier, S.; Cho, K.; Grzesiek, S.; Bruschweiler, R.; Blackledge, M. *Proc. Natl. Acad. Sci. U.S.A.* **2005**, *102*, 13885−13890.
(18) Briggman, K. B.; Tolman, J. R. *J. Am. Chem. Soc.* **2003**, *125*, 10164−10165.
(19) Hoch, J. C.; Dobson, C. M.; Karplus, M. *Biochemistry* **1985**, *24*, 3831−3841.
(20) Gibbons, W. A.; Nemethy, G.; Stern, A.; Craig, L. C. *Proc. Natl. Acad. Sci. U.S.A.* **1970**, *67*, 239−&.
(21) Bruschweiler, R.; Case, D. A. *J. Am. Chem. Soc.* **1994**, *116*, 11199−11200.
(22) Case, D. A.; Scheurer, C.; Bruschweiler, R. *J. Am. Chem. Soc.* **2000**, *122*, 10390−10397.
(23) Schmidt, J. M.; Blumel, M.; Lohr, F.; Ruterjans, H. *J. Biomol. NMR* **1999**, *14*, 1−12.
(24) Montelione, G. T.; Wagner, G. *J. Am. Chem. Soc.* **1989**, *111*, 5474−5475.
(25) Biamonti, C.; Rios, C. B.; Lyons, B. A.; Montelione, G. T. *Adv. Biophys. Chem.* **1994**, *4*, 51−120.
(26) Bax, A.; Vuister, G. W.; Grzesiek, S.; Delaglio, F.; Wang, A. C.; Tschudin, R.; Zhu, G. *Methods Enzymol.* **1994**, *239*, 79−105.
(27) Lohr, F.; Schmidt, J. M.; Ruterjans, H. *J. Am. Chem. Soc.* **1999**, *121*, 11821−11826.
(28) Lohr, F.; Ruterjans, H. *J. Biomol. NMR* **1999**, *13*, 263−274.
(29) Wang, A. C.; Bax, A. *J. Am. Chem. Soc.* **1996**, *118*, 2483−2494.
(30) Hu, J. S.; Bax, A. *J. Am. Chem. Soc.* **1997**, *119*, 6360−6368.
(31) Harbison, G. S. *J. Am. Chem. Soc.* **1993**, *115*, 3026−3027.
(32) Rexroth, A.; Schmidt, P.; Szalma, S.; Geppert, T.; Schwalbe, H.; Griesinger, C. *J. Am. Chem. Soc.* **1995**, *117*, 10389−10390.
(33) Griesinger, C.; Sørensen, O. W.; Ernst, R. R. *J. Magn. Reson.* **1987**, *75*, 474−492.
(34) Ulmer, T. S.; Ramirez, B. E.; Delaglio, F.; Bax, A. *J. Am. Chem. Soc.* **2003**, *125*, 9179−9191.
(35) Derrick, J. P.; Wigley, D. B. *J. Mol. Biol.* **1994**, *243*, 906−918.

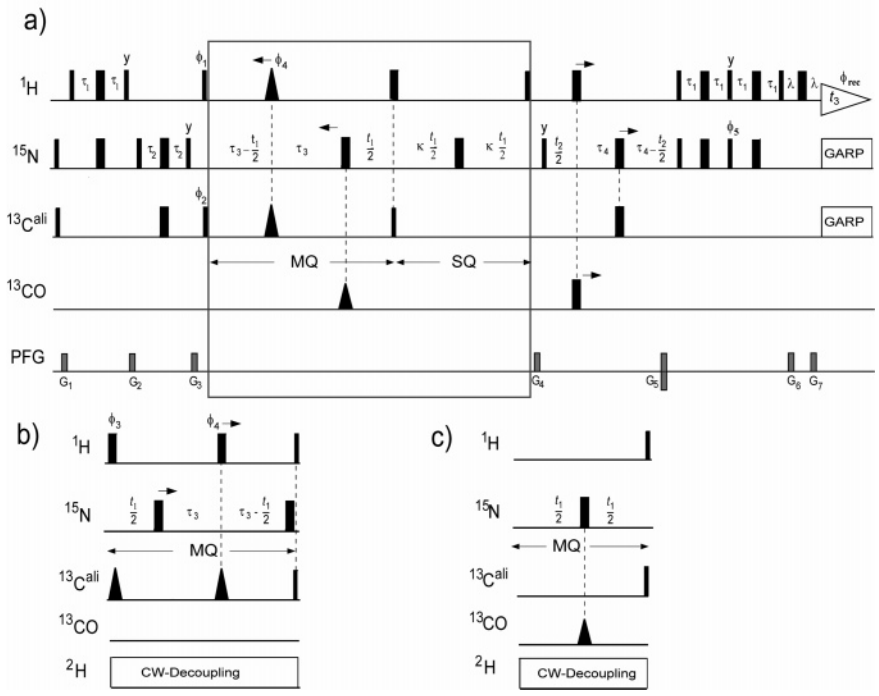

Figure 1. Pulse diagrams of the 3D MQ(^{1}H^N,^{13}C$^\alpha$)-HNCA experiments for measurements of $^3J_{H^N,H^\alpha}$, $^3J_{H^N,C'}$, and $^3J_{H^N,C^\beta}$. For $^3J_{H^N,H^\alpha}$, pulse scheme (a) is used. For measurement of $^3J_{H^N,C'}$, the boxed element in (a) is substituted by the element shown in (b) and likewise, for measurement of $^3J_{H^N,C^\beta}$, by the element shown in (c). For (b) and (c), perdeuteration of non-exchangeable protons is required. The representation shown is schematic, without marking of delays for ensuring zero phase. A more detailed version of the pulse sequence, including such delays, is provided in the Supporting Information, Figure S4. Narrow and wide filled bars indicate nonselective 90° and 180° pulses. Triangular-shaped ^{13}C′ pulses represent selective 180° Gaussian pulses; triangular ^{13}C^{ali} pulses are broadband aliphatic inversion/refocusing pulses. The triangular pulse on ^{1}H depicts an H^N-selective REBURP pulse,[36] carefully adjusted to invert the H^N but not the H$^\alpha$ spins. Unless indicated otherwise, all radio frequency pulses are applied with phase *x*. Phase cycling: $\phi_3 = \{x, x, x, x, -x, -x, -x, -x\}$; $\phi_4 = \{x, -x, x, -x\}$; $\phi_5 = y$; $\phi_{rec} = \{x, -x, -x, x\}$. For spectrum A: $\phi_1 = \{x, x, -x, -x\}$; $\phi_2 = \{x, -x, x, -x\}$. For spectrum B: $\phi_1 = \{y, y, -y, -y\}$; $\phi_2 = \{y, -y, y, -y\}$. A − B (A + B) selects DQ (ZQ) components.[32] Delay values: $\tau_1 = 2.6$ ms, $\tau_2 = 13.7$ ms, $\tau_3 = 13$ ms in (a) and 27 ms in (b), $\tau_4 = 1/(4J_{N,C^\alpha}) = 13.5$ ms, $\lambda = 320$ μs. Pulsed field gradients, indicated on the line marked PFG, are applied along the *x*-, *y*-, and *z*-axis with the following duration/strength: G$_1$, 500 μs, 18 G/cm; G$_2$, 300 μs, 36 G/cm; G$_3$, 500 μs, 18 G/cm; G$_4$, 250 μs, 15 G/cm; G$_5$, 3400 μs, −30 G/cm; G$_6$, 144.75 μs, −30 G/cm; G$_7$, 200 μs, 30 G/cm. Quadrature detection in the MQ(t_1) dimension is achieved in the regular States−TPPI manner, simultaneously incrementing ϕ_1 and ϕ_2; quadrature in the ^{15}N dimension is achieved by the Rance−Kay method,[37] inverting G$_5$ and ϕ_5.

followed by zero-filling 1024 × 256 × 1024 complex points and Fourier transformation.

$^3J_{H^N,H^\alpha}$ couplings were independently obtained from nonlinear fitting of the intensities observed in a series of 2D CT-HMQC-J experiments,[38] with total durations for the time where H^N magnetization is subject to $^3J_{H^N,H^\alpha}$ dephasing, 2Δ + 4T, of 45, 60, 80, 100, 120, and 140 ms.

In addition to the new ZQ/DQ measurements, $^3J_{H^N,C'}$ and $^3J_{H^N,C^\beta}$ couplings were also obtained from 3D HNCA-based E.COSY-type experiments,[24] adapted for measurement of $^3J_{H^N,C'}$[39] and $^3J_{H^N,C^\beta}$ couplings. For measurement of the latter couplings, a small flip angle (15°) pulse was used at the end of C$^\alpha$ evolution, rather than a C$^\alpha$-selective pulse,[29] which would have interfered with measurement of $^3J_{H^N,C^\beta}$ of Thr and Ser residues, whose C$^\beta$ resonate close to the C$^\alpha$ region. The 3D E.COSY data sets were recorded with $t_{1max} = 56.5$ ms, $t_{2max} = 18.8$ ms, $t_{3max} = 263$ ms, an interscan delay of 0.8 s, and 8 scans per FID, corresponding to 3D matrices consisting of 256 (t_1) × 32 (t_2) × 4096 (t_3) complex points, subsequently zero-filled to 512 × 64 × 8192 complex points. All spectra were processed and analyzed using the software package NMRPipe.[40] Peak positions were determined by parabolic interpolation.

Results and Discussion

Any observed *J* splitting is reduced relative to the true *J* value by an effect that finds its origin in differential relaxation rates of coherences that are in-phase or antiphase with respect to the passive spin, X, whose couplings are being sought.[31] Although numerous methods for ^3J-coupling measurement in proteins have been proposed over the past few decades, the vast majority of these are affected by this differential relaxation rate, contributing to an error that is difficult to quantify. Methods based on the multiple-quantum (MQ) approach, proposed by the Griesinger laboratory,[32] greatly alleviate the severity of this effect, however. For an I,S two-spin coherence, the *J* splitting due to interaction with spin X equals $J_{I,X} \pm J_{S,X}$. Provided that $|J_{I,X} \pm J_{S,X}| > R_{1X}/2\pi$, the apparent *J*-modulation frequency of MQ (I,S) coherence, coupled to spin X, is given by

$$(J_{I,X} \pm J_{S,X})_{app} = \sqrt{(J_{I,X} \pm J_{S,X})^2 - (R_{1X}/2\pi)^2} \qquad (1)$$

where R_{1X} is the longitudinal relaxation rate of X as observed in a selective inversion−recovery experiment, i.e., including *J*(0) spectral density contributions. For $|J_{I,X} \pm J_{S,X}| \gg R_{1X}/2\pi$, the impact of longitudinal X-spin relaxation on the difference, $|J_{I,X} + J_{S,X}| - |J_{I,X} - J_{S,X}|$, is minimal, which then allows reliable extraction of both $J_{I,X}$ and $J_{S,X}$ from the sum and difference of $|J_{I,X} + J_{S,X}|$ and $|J_{I,X} - J_{S,X}|$. Below, we describe a constant-time modification of Rexroth's original experiment,[32] yielding

(36) Geen, H.; Freeman, R. *J. Magn. Reson.* **1991**, *93*, 93−141.
(37) Kay, L. E.; Keifer, P.; Saarinen, T. *J. Am. Chem. Soc.* **1992**, *114*, 10663−10665.
(38) Kuboniwa, H.; Grzesiek, S.; Delaglio, F.; Bax, A. *J. Biomol. NMR* **1994**, *4*, 871−878.
(39) Wang, A. C.; Bax, A. *J. Am. Chem. Soc.* **1995**, *117*, 1810−1813.
(40) Delaglio, F.; Grzesiek, S.; Vuister, G. W.; Zhu, G.; Pfeifer, J.; Bax, A. *J. Biomol. NMR* **1995**, *6*, 277−293.

measurement of $^3J_{H^N,H^\alpha}$ at increased resolution, and extend the MQ concept to measurement of $^3J_{H^N,C^\beta}$ and $^3J_{H^N,C'}$ couplings.

Multiple-Quantum Measurement of ^3J-Couplings. Figure 1 shows three pulse sequences, based on the MQ concept, for measurement of $^3J_{H^N,H^\alpha}$, $^3J_{H^N,C^\beta}$, and $^3J_{H^N,C'}$. In these experiments, zero-quantum (ZQ) and double-quantum (DQ) coherence between the amide proton and intraresidue $^{13}C^\alpha$ evolves in the presence of a nonperturbed third spin, X, where X is H^α, C^β, or C'. Whereas the ZQ term is then modulated by $\cos[\pi(^1J_{C^\alpha,X} - {}^3J_{H^N,X})t_1]$, the DQ signal will be modulated by $\cos[\pi(^1J_{C^\alpha,X} + {}^3J_{H^N,X})t_1]$. Considering that $^1J_{C^\alpha,X} \gg {}^3J_{H^N,X}$, this approach yields relatively large, resolvable splittings of both the DQ and ZQ signals, and the difference in their splittings equals $2^3J_{H^N,X}$ (for $X = C'$, C^β) or $2(1 + \kappa)^3J_{H^N,X}$ (for $X = H^\alpha$).

In general terms, all three experiments can be described by the following coherence pathway:

$$^1H \rightarrow {}^{15}N \rightarrow MQ[^1H^N,{}^{13}C^\alpha](E/2 \pm X_z) \exp\{-i(\Omega^{MQ} \pm \pi J_{MQ})t_1 - R_{MQ}T_{MQ}\} \rightarrow$$

$$SQ[^1H^N](E/2 \pm X_z) \exp\{(-i(-\Omega^{H^N} \pm \pi J_{H^N,X}) - R_{SQ})\kappa t_1\} \rightarrow$$

$$^{15}N \exp\{-i\Omega^N t_2 - 2R_2{}^N\tau_4\} \rightarrow {}^1H \exp\{(-i\Omega^H - R_2{}^H)t_3\} \quad (2)$$

where E is the unity operator; MQ denotes the DQ or ZQ operator; J_{DQ} and J_{ZQ} are $J_{H^N,X} + J_{C^\alpha,X}$ and $J_{H^N,X} - J_{C^\alpha,X}$, respectively; Ω^{C^α}, Ω^{H^N}, and Ω^N are the angular $^{13}C^\alpha$, $^1H^N$, and ^{15}N chemical shift frequencies, respectively; $\Omega^{DQ} = \Omega^{H^N} + \Omega^{C^\alpha}$ and $\Omega^{ZQ} = \Omega^{H^N} - \Omega^{C^\alpha;}$ R_{MQ} is the MQ relaxation rate, R_{SQ} the transverse $^1H^N$ relaxation rate, and $R_2{}^N$ and $R_2{}^H$ the transverse ^{15}N and $^1H^N$ relaxation rates; T_{MQ} is the total MQ[$^1H^N$,$^{13}C^\alpha$] duration; and $2\tau_4$ is the duration of the constant-time ^{15}N t_2 evolution period. For the schemes of Figure 1a,b, T_{MQ} equals the duration of the constant-time MQ evolution period; for Figure 1c, $T_{MQ} = t_1$. Spin X refers to $^1H^\alpha$, $^{13}C'$, and $^{13}C^\beta$ for the schemes of Figure 1a−c, respectively. The intermediate conversion to single-quantum coherence, SQ[$^1H^N$], between MQ and ^{15}N takes place only in the scheme of Figure 1a, with $\kappa > 0$; for the other experiments, MQ is converted directly into ^{15}N. The SQ[$^1H^N$] element extends the evolution under the $^3J_{H^N,H^\alpha}$ Hamiltonian by κt_1, and $^1H^N$ chemical-shift evolution continues after the MQ evolution. This then yields effective chemical shift modulation frequencies of $\Omega^{C^\alpha} + \Omega^{H^N} - \kappa\Omega^{H^N}$ for the double-quantum component and $\Omega^{C^\alpha} - \Omega^{H^N} + \kappa\Omega^{H^N}$ for the zero-quantum signal.[32] This has the net effect of scaling the contribution of $^3J_{H^N,H^\alpha}$ to the apparent J splitting in the MQ dimension:

$$J_{MQ}{}^{app} = {}^1J_{C\alpha,H\alpha} \pm (1 + \kappa)^3J_{H^N,H\alpha} \quad (3)$$

where the + and − signs apply for the double- and zero-quantum spectra, respectively. Note that increasing the contribution of $^3J_{H^N,H^\alpha}$ to the MQ splitting by increasing κ also increases the line widths, owing to the relaxation term R_{SQ} that is active during κt_1, albeit that better effective resolution is attainable because the total time during which $^3J_{H^N,H^\alpha}$ evolves becomes longer than the 28 ms constant-time duration applicable for $\kappa = 0$. In practice, the additional relaxation results in an upper limit $\kappa \leq 2$. For the $^3J_{H^N,C'}$ and $^3J_{H^N,C^\beta}$ measurements, carried out for the perdeuterated sample, the $^{13}C^\alpha-{}^1H^N$ multiple-quantum relaxation rate is no longer dominated by the $^{13}C^\alpha-{}^1H$ dipolar contribution, and longer sampling in the t_1 dimension can be used for enhancing resolution instead of using the additional SQ period, i.e., keeping $\kappa = 0$.

The pulse sequences shown in Figure 1 at first sight may appear to contain more than the absolute minimum number of pulses needed for selecting the desired coherence transfer pathway. However, these additional pulses are needed to ensure that at time $t_1 = 0$, there has been zero evolution caused by J coupling and by ^1H and ^{13}C chemical shifts, i.e., that in the multiple-quantum dimension the signals are modulated by pure cosine (or sine) terms. Note that any dephasing prior to $t_1 = 0$ cannot easily be accounted for by common linearly frequency-dependent phase correction, and any J-evolution prior to $t_1 = 0$ would lead to relative phase errors within a given multiplet, which can significantly impact the extraction of J-coupling values.[41] Details on delay durations and pulses, required to ensure minimal dephasing at $t_1 = 0$, are given in the Supporting Information.

The pulse scheme of Figure 1a converts the original experiment of Rexroth et al. into a constant-time (CT) experiment with a $^{13}C^\alpha$ CT duration of $1/{}^1J_{C^\alpha,C^\beta} \approx 28$ ms, thereby removing $^1J_{C^\alpha,C^\beta}$ splittings and enhancing resolution. Figure 2 shows cross sections orthogonal to the ^{15}N axis through the multiple-quantum spectra recorded with the scheme of Figure 1a, for $\kappa = 1$ (Figure 2a) and $\kappa = 2$ (Figure 2b). For each of these spectra, the cross section through the double-quantum correlation of residue T49 has been superimposed on the zero-quantum doublet. The differences in splitting for the spectra of Figure 2a,b equal $4^3J_{H^N,H^\alpha}$ and $6^3J_{H^N,H^\alpha}$, respectively. ^3J values for GB3 are presented in the Supporting Information.

The 3D CT-MQ($^1H^N$,$^{13}C^\alpha$)-HNCA experiment for measurement of $^3J_{H^N,C'}$ (Figure 1b) has been designed for application to samples where the ^{13}C-attached hydrogens are substituted by deuterium, obviating the need of $^1H^\alpha$ decoupling during the CT $^1H^N-{}^{13}C^\alpha$ multiple-quantum evolution period. Analogous to the scheme of Figure 1a, CT evolution eliminates $^1J_{C^\alpha,C^\beta}$ splittings in the F_1 dimension. Considering the long $^{13}C^\alpha$ transverse relaxation time of the perdeuterated GB3 sample used for this measurement, a longer CT duration of $2/{}^1J_{C^\alpha,C^\beta} \approx 56$ ms is used, increasing spectral resolution in the multiple-quantum dimension (Figure 2c) without adversely impacting sensitivity. Note that, however, at higher multiples of $1/{}^1J_{C^\alpha,C^\beta}$, long-range $^{13}C-{}^{13}C$ J-dephasing can lead to considerable signal loss.

The MQ($^1H^N$,$^{13}C^\alpha$)-HNCA experiment of Figure 1c is aimed at measurement of $^3J_{H^N,C^\beta}$. In contrast to the experiments of Figure 1a,b, $^1J_{C^\alpha,C^\beta}$ is not removed by performing the experiment in a constant-time manner. Instead, $^1J_{C^\alpha,C^\beta}$ becomes the dominant contribution to the MQ($^1H^N$,$^{13}C^\alpha$) splitting, to which $^3J_{H^N,C^\beta}$ is either added or subtracted (Figure 2d).

Note that, although the three multiple-quantum experiments of Figure 1 are intended for measurement of three-bond intraresidue J couplings, the connectivity between $^{15}N_i$ and $^{13}C^\alpha_{i-1}$, resulting from $^2J_{N,C^\alpha}$ in HNCA-type experiments, also yields correlations to $^{13}C^\alpha_{i-1}$, and therefore to $^4J_{H^N,H^\alpha}$ (Figure 1a), $^2J_{H^N,C'}$ (Figure 1b), and $^4J_{H^N,C^\beta}$ (Figure 1c). Although the presence of these sequential $^2J_{N,C^\alpha}$-mediated correlations does

(41) Kontaxis, G.; Clore, G. M.; Bax, A. *J. Magn. Reson.* **2000**, *143*, 184−196.

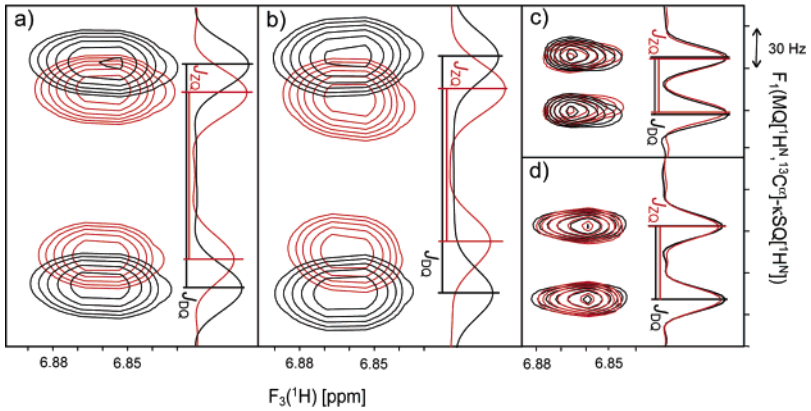

Figure 2. Overlays of two-dimensional cross sections taken through the 3D multiple-quantum spectra recorded for the protein GB3 with the pulse schemes of (a,b) Figure 1a ($\kappa = 1$ for (a); $\kappa = 2$ for (b)), (c) Figure 1b, and (d) Figure 1c. Cross sections through the multiplets corresponding to residue T49 are taken orthogonal to the ^{15}N axis and display the superimposed H^N-C^α double-quantum (black) and zero-quantum (red) frequencies, split by (a) $^1J_{C^\alpha,H^\alpha} \pm 2^3J_{H^N,H^\alpha}$, (b) $^1J_{C^\alpha,H^\alpha} \pm 3^3J_{H^N,H^\alpha}$, (c) $^1J_{C^\alpha,C^\beta} \pm {}^3J_{H^N,C^\beta}$, and (d) $^1J_{C^\alpha,C'} \pm {}^3J_{H^N,C'}$, where the + and − signs refer to the double-quantum (black) and zero-quantum (red) signals, respectively.

not directly impact the measured couplings, it can result in resonance overlap and some attenuation of the intraresidue correlations of interest. Use of τ_2 and τ_4 durations of ca. 13.5 ms, slightly longer than commonly used in regular HNCA experiments, where observation of this sequential connectivity is desirable, minimizes the intensity of these sequential connectivities while increasing the sensitivity for the intraresidue correlations of interest.

Validation of Multiple-Quantum *J*-Measurements. Although the multiple-quantum experiments are intrinsically much less affected by the finite lifetime of the passively coupled spin,[32] the presence of other systematic errors cannot be excluded *a priori*. We therefore compare these measurements with results from well-established *J*-modulation ($^3J_{H^N,H^\alpha}$) and E.COSY experiments ($^3J_{H^N,C^\beta}$ and $^3J_{H^N,C'}$), with the anticipation that these standard experiments may show slightly reduced couplings when no correction for the finite lifetime of the passive spin is used. In the absence of phase or line shape distortion, the precision at which a peak position can be determined equals approximately LW/(2S/N), where LW is the line width at half-height and S/N the signal-to-noise ratio.[41] Using this relation, we find lower limits for the propagated uncertainties of 0.08 Hz for $^3J_{H^N,H^\alpha}$ at $\kappa = 1$ and 0.07 Hz for $\kappa = 2$ (Supporting Information, Table S4). With the pairwise rmsd between the $\kappa = 1$ and $\kappa = 2$ measurements being 0.15 Hz, this points to self-consistency of the two multiple-quantum measurements of $^3J_{H^N,H^\alpha}$. These couplings also show close agreement with $^3J_{H^N,H^\alpha}$ couplings measured from a series of $^3J_{H^N,H^\alpha}$-modulated HMQC experiments (Figure 3a). The pairwise rmsd between the averaged MQ sets of $^3J_{H^N,H^\alpha}$ couplings and those obtained from $^3J_{H^N,H^\alpha}$ modulation equals 0.28 Hz, indicating a random error of 0.14 Hz in their averaged values. Although this pairwise rmsd is somewhat larger than expected on the basis of their statistical minimal uncertainties, the random uncertainty in the averaged values is much smaller than the rmsd obtained when fitting these data to a Karplus equation (see below) and, therefore, will not limit our analysis.

Based on line width and S/N for $^3J_{H^N,C'}$, the experimental random error in the multiple-quantum-based measurement (Figure 1b) is ~0.16 Hz, whereas smaller random errors (~0.06 Hz) are obtained with the HNCA[CO] E.COSY measurement. With the pairwise rmsd between the two sets of independent measurements being 0.19 Hz (Figure 3b), this points to the absence of significant systematic errors in either measurement and a random error of 0.10 Hz in their averaged values.

For the multiple-quantum $^3J_{H^N,C^\beta}$ measurement, the measurement precision based on line width and signal-to-noise ratio is estimated at 0.10 Hz. Comparison with values measured from the HNCA[CB] E.COSY experiment shows a small systematic difference between the two sets, with the E.COSY experiments being, on average, 6% smaller (Figure 3c). The smaller E.COSY value is anticipated on the basis of the non-negligible effect of the 15° ^{13}C pulse at the end of the $^{13}C^\alpha$ evolution period on the passive spin ($^{13}C^\beta$), accounting for a 3−4% reduction in the E.COSY $^3J_{H^N,C^\beta}$ value, with the remainder attributed to the finite $^{13}C^\beta$ T_1 value. After the E.COSY $^3J_{H^N,C^\beta}$ values are increased by 6%, the pairwise rmsd between the two sets of measurements equals 0.14 Hz, indicating a random error of ~0.07 Hz in the averaged values, used for all further analyses.

The exceptionally small error in the $^3J_{H^N,C^\beta}$ and $^3J_{H^N,C'}$ measurements can be attributed to the fact that a perdeuterated protein was used, resulting in favorable relaxation behavior of the $^1H^N-^{13}C^\alpha$ multiple-quantum coherence and narrowing of H^N line widths in the E.COSY-type experiments. The use of a 15° flip angle pulse after $^{13}C^\alpha$ evolution rather than a selective $^{13}C^\alpha$ pulse lowers the signal-to-noise ratio by 75%. However, the higher sensitivity afforded by the use of perdeuteration, together with GB3's small size and the high sample concentration, made it preferable to use this small flip angle (15°) pulse over a band-selective $^{13}C^\alpha$ pulse, which would have interfered with measurements for Thr and Ser residues.[29]

The pulse sequences presented in Figure 1 were key for eliminating the possibility of systematic errors caused by the finite lifetime of the passive spin in the commonly used E.COSY and *J*-modulation measurements. Our results indicate that, at least for small proteins such as GB3, this systematic error is indeed smaller than the random measurement error. Considering that the precision of the ^3J measurement in the conventional E.COSY and *J*-modulation experiments is comparable to that obtained with the new experiments of Figure 1, averaging of the values obtained from these independent measurements yields the most reliable ^3J couplings.

Fits of Karplus Equations to a Static Protein Structure. Karplus equations relate the three-bond scalar couplings *J* to

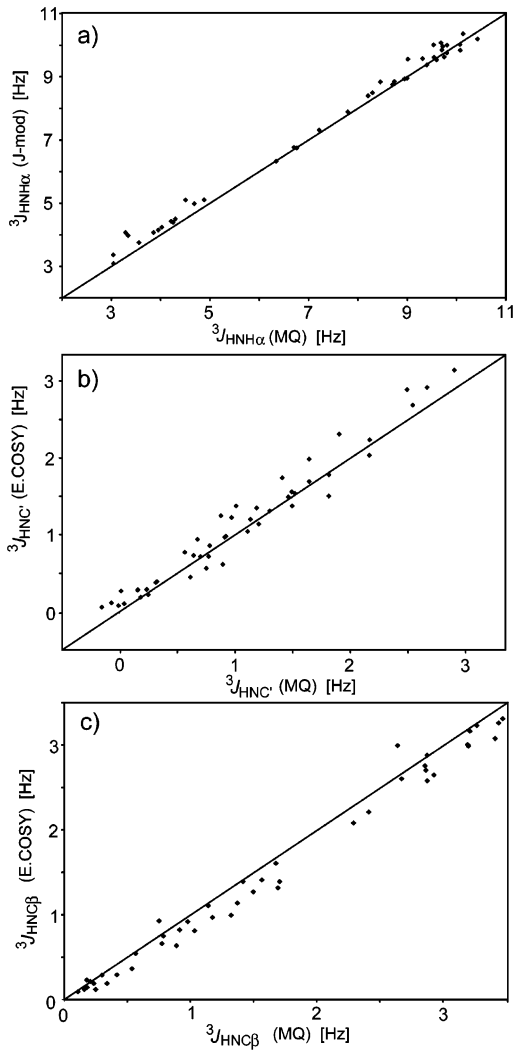

Figure 3. Comparison of ^3J couplings in GB3 measured with the multiple-quantum experiments of Figure 1 and values measured using conventional experiments. (a) Values measured with the pulse scheme of Figure 1a (averaged over $\kappa = 1$ and $\kappa = 2$) versus values measured by *J*-modulated CT-heteronuclear multiple-quantum coherence (HMQC).[38] Based on Monte Carlo analysis, adding random noise to the peak intensities, the CT-HMQC-derived $^3J_{H^N,H^\alpha}$ values have a lower limit random error of 0.13 Hz. (b) Comparison of $^3J_{H^N,C'}$ measured with the pulse scheme of Figure 1b with those from HNCA[C′]-E.COSY. (c) Comparison of $^3J_{H^N,C^\beta}$ measured with the pulse scheme of Figure 1c with those from HNCA[C^β]-E.COSY.

their intervening dihedral angles, θ.[42] Many empirically determined parameter sets have been presented over the years for the six different couplings that relate to the peptide torsion angle ϕ.[23,29,30,43−45] The vast majority of prior parametrizations for the relation between $^3J_{H^N,H^\alpha}$, $^3J_{H^N,C'}$ and $^3J_{H^N,C^\beta}$ and intervening dihedral angles are based on X-ray coordinates of the backbone atoms to derive the $C'_{i-1}-N_i-C^\alpha_i-C'_i$ torsion angle, ϕ, and utilize $\theta = \phi - 60°$, $\theta = \phi + 180°$, and $\theta = \phi + 60°$ as the respective dihedral angles. Our present set of *J* couplings is among the highest in measured precision available to date; moreover, very high resolution (1.1-Å) X-ray[35] and NMR[34] structures are available for GB3. In addition, one of the NMR structures (PDB entry 2OED), calculated on the basis of a very large number of RDCs, recorded in five different media, has been refined with relaxed geometric restraints, allowing the amide N−H vector to bend out of the peptide plane. A very similar parameter set was used in deriving the GB3 ensemble structure,[16] resulting in comparable deviations from idealized geometry. It is therefore interesting to evaluate whether the improved measurement precision and the high resolution of the reference structure result in better fits to the Karplus equations than available previously, and whether these equations provide a better match to the experimental couplings when using the ϕ-derived dihedral angles or the actual dihedral angles computed on the basis of the ^{1}H coordinates in the RDC-refined structure. When comparing the dihedral angles intervening the ^3J-coupled nuclei in the NMR structure of GB3 (PDB entry 2OED) with the corresponding angles in the analogous structure where hydrogens and C^β carbons are first removed and then added in their idealized positions, the pairwise rmsd between the applicable dihedral angles equals 5.0° for $^3J_{H^N,H^\alpha}$, 4.2° for $^3J_{H^N,C'}$, and 4.6° for $^3J_{H^N,C^\beta}$. The pairwise rmsd between the ϕ angles of the NMR and crystal structures (3.4°) is somewhat smaller.

With the exception of two residues (L12 and D40), previously identified on the basis of ^{15}N relaxation measurements as being subject to highly elevated backbone dynamics,[46] all non-Gly residues for which ^3J couplings could be measured are included in the Karplus curve parametrization. In addition, considering that GB3 contains only a single non-Gly residue with a positive ϕ angle, data from all three non-Gly residues with $\phi > 0$ in ubiquitin, for which very precise $^3J_{H^N,H^\alpha}$, $^3J_{H^N,C'}$, and $^3J_{H^N,C^\beta}$ values were reported previously,[29] were added to the input data, resulting in a better definition of the Karplus curves in the positive ϕ region.

Although the Karplus coefficients obtained when fitting the same sets of $^3J_{H^N,H^\alpha}$, $^3J_{H^N,C'}$, and $^3J_{H^N,C^\beta}$ couplings to their respective dihedral angles are very similar to one another when using different input structures (Supporting Information, Table S6), the fit to the RDC-refined structure (PDB entry 2OED, calculated in the absence of ^3J-coupling input restraints) is superior for all three coupling types. The corresponding Karplus coefficients are listed in Table 1. Not only is there an improvement in the fit when using the ϕ angles of the NMR structure over those of the X-ray structure, in both cases adding the protons in idealized positions (Figure 4), but a considerably larger improvement in the fit is obtained when the experimentally derived hydrogen positions are used for calculating the applicable dihedral angles. Remarkably, the agreement further improves when fitting the ^3J couplings to a dynamic ensemble,[16] calculated from the same input parameters as the regular RDC-refined NMR structure supplemented with experimental ^{15}N relaxation-derived order parameters, S^2,[46] and X-ray-derived temperature factors.[35] Figure 4 indicates that, for both the single structure and the ensemble structure, an optimal fit is obtained for each of the three coupling types when the hydrogen positions are close to 100% of the full deviation from idealized geometry, obtained in the RDC-refined structures which are generated with attenuated geometric restraints for H^N positioning.[16,34]

Impact of Backbone Dynamics on Fit to Karplus Curves. When parametrizing Karplus equations, motional averaging

(42) Karplus, M. *J. Phys. Chem.* **1963**, *85*, 2870−2871.
(43) Bystrov, V. F. *Prog. NMR Spectrosc.* **1976**, *10*, 41−82.
(44) Pardi, A.; Billeter, M.; Wüthrich, K. *J. Mol. Biol.* **1984**, *180*, 741−751.
(45) Perez, C.; Lohr, F.; Ruterjans, H.; Schmidt, J. M. *J. Am. Chem. Soc.* **2001**, *123*, 7081−7093.
(46) Hall, J. B.; Fushman, D. *J. Biomol. NMR* **2003**, *27*, 261−275.

Table 1. Karplus Coefficients and Statistical Values from Fits[a]

fitting model[b]	^3J type	A (Hz)	B (Hz)	C (Hz)	rmsd (Hz)
rigid	H^N,H^α	7.97	−1.26	0.63	0.42
rigid	H^N,C'	4.12	−1.10	0.11	0.31
rigid	H^N,C^β	3. 51	−0.53	0.14	0.25
motion	H^N,H^α	8.69	−1.14	0.39	0.38[c]
motion	H^N,C'	4.53	−1.09	−0.09	0.31[c]
motion	H^N,C^β	3.85	−0.47	−0.08	0.23[c]
ensemble[d]	H^N,H^α	8.40	−1.36	0.33	0.36
ensemble[d]	H^N,C'	4.36	−1.08	−0.01	0.30
ensemble[d]	H^N,C^β	3.71	−0.59	0.08	0.22

[a] Reported values correspond to the fits of the ^3J values listed in Supporting Information Table S5 to the NMR structure (PDB entry 2OED) of GB3. Values for three non-Gly residues with positive ϕ angles in ubiquitin (A46, N60, and E64), together with dihedral angles from its NMR-refined X-ray structure,[30] were also included in the fit. [b] "Rigid" refers to conventional singular value decomposition (SVD) fitting of observed ^3J couplings (all values except for dynamically disordered L12 and D40) to a static structure. "Motion" refers to the results obtained when using eq 5 and A coefficients fixed at values obtained when using a separate fit to 35 GB3 plus 3 ubiquitin residues that fit within 1.5 standard deviations to a static model, and having ^{15}N-relaxation-derived $S^2 \geq 0.75$, assuming a uniform $\sigma = 10°$. [c] Allowing for residue-specific σ values, i.e., using 56 instead of 9 variable parameters in the fit. [d] Karplus coefficients are derived from a fit to Karplus equations for each of the 160 ensemble conformers. With the observed J couplings being linear averages over the coupling of each conformer, the $N \times M$ linear equation system (where N is the number of coupling types and M is the number of ϕ angles evaluated) to be minimized is given by $J^{ik,\text{observed}} = (1/P)\sum_{l=1}^{P} J^{ikl} = A_k\langle\cos^2(\phi_{il} + \eta_{ikl})\rangle + B_k\langle\cos(\phi_{il} + \eta_{ikl})\rangle + C_k$, where $i \in \{1, ..., M\}$, $k \in \{1, ..., N\}$, and l sums over P ensemble conformers. The number of adjustable parameters equals three for each Karplus equation.

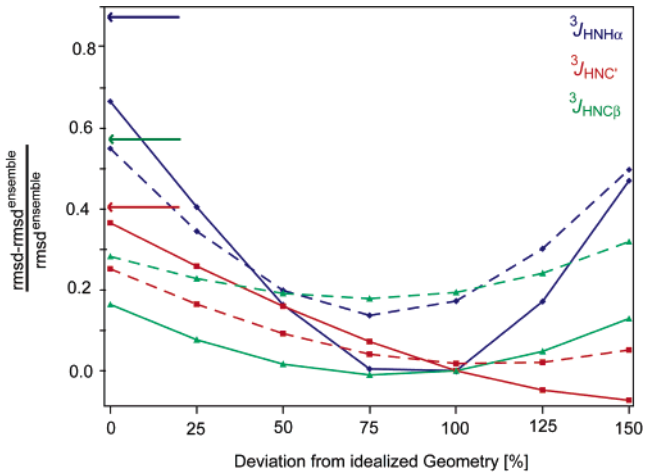

Figure 4. Relative root-mean-square deviations (rmsd) between $^3J_{H^N,H^\alpha}$ (blue), $^3J_{H^N,C'}$ (red), and $^3J_{H^N,C^\beta}$ (green) and their respective optimized static Karplus curves (eq 4 with $\sigma = 0$) when fit to the NMR structure of GB3 (PDB code 2OED) (dashed lines) or to the 160-member dynamic ensemble of NMR structures (solid lines), as a function of hydrogen positioning. A 0% deviation corresponds to structures where H^N, H^α, and C^β are in their idealized positions, and 100% corresponds to hydrogens in their RDC-derived positions, with a linear scaling of the applicable dihedral angles for intermediate percentages. The value rmsd^{nmr} refers to the rmsd between the observed couplings and those averaged for the ensemble of NMR structures when using Karplus parameters optimized for this ensemble (Supporting Information, Table S7; rmsd^{nmr} = 0.36, 0.30, and 0.22 Hz for $^3J_{H^N,H^\alpha}$, $^3J_{H^N,C'}$ and $^3J_{H^N,C^\beta}$, respectively). Arrows mark the fractional increase in rmsd when Karplus equations are optimized on the basis of the 1IGD X-ray coordinates, with hydrogens added in their idealized positions. In the fits, the highly mobile GB3 residues L12 and D40 were excluded, and the three human ubiquitin residues with positive ϕ values (A46, N60, and E64; angles from NMR-refined X-ray structure[30]) were included for tighter restriction.

effects are automatically absorbed in the coefficients of these best-fitted Karplus equations.[21] Any measured J coupling represents the time-average of the instantaneous J values. These instantaneous J couplings vary with time due to the angular fluctuations of the intervening dihedral angle, which occurs on a time scale faster than the measurement.[19,20]

Assuming averaging over a Gaussian-distributed range of angles, with a standard deviation σ around an average value θ, for $\sigma \ll \pi$ the time-averaged J value can simply be expressed as[21]

$$J(\theta,\sigma) = A\exp(-2\sigma^2)\cos^2\theta + B\exp(-\sigma^2/2)\cos\theta + (A/2)(1 - \exp(-2\sigma^2)) + C \quad (4)$$

In this notation, for a perfectly rigid molecule, i.e., when $\sigma = 0$, the coefficients of the resulting quadratic equation in terms of $\cos\theta$ become the standard Karplus coefficients, commonly referred to as A, B, and C. When Karplus equations are parametrized on the basis of experimentally determined ^3J couplings in a protein, the extracted coefficients reflect an average over the set of site-specific values of $A\exp(-2\sigma^2)$, $B(-\sigma^2/2)$, and $(A/2)(1 - \exp(-2\sigma^2)) + C$.

In proteins, several three-bond J couplings define the backbone torsion angle ϕ. Assuming time-independent covalent bond angles at the C^α site, Karplus equations for each coupling type depend on the same set of ϕ and σ values. An $N \times M$ nonlinear equation system (where N is the number of coupling types and M is the number of ϕ angles evaluated) can then be solved by best-fitting

$$J^{i,k}(\phi_i,\sigma_i) = A_k\exp(-2\sigma_i^2)\cos^2(\phi_i + \eta_{ik}) + B_k\exp(-\sigma_i^2/2)\cos(\phi_i + \eta_{ik}) + (A_k/2)(1 - \exp(-2\sigma_i^2)) + C_k \quad (5)$$

where $i \in \{1, ..., M\}$ and $k \in \{1, ..., N\}$. For planar peptide bond geometry and ideal tetrahedral geometry at C^α, η_{ik} would equal $-\pi/3$ for $^3J_{H^N,H^\alpha}$, π for $^3J_{H^N,C'}$, or $\pi/3$ for $^3J_{H^N,C^\beta}$. In this study, η_{ik} values are taken either from structures to which protons were added in idealized positions or from the NMR structure of GB3, calculated by inclusion of RDCs, where the amide proton is not forced to be in the peptide plane. The deviations of η from the canonical values are small. For example, a pairwise rmsd of 5.6° is found when comparing the $H^N-N-C^\alpha-H^\alpha$ dihedral angles of NMR structures with experimental ^{1}H positions, with those where the ^{1}H coordinates are first deleted and then re-added assuming idealized geometry. Nevertheless, as shown below, use of the experimental η values results in significantly better fits to the Karplus equations.

With three different ^3J couplings measured for each of N residues in GB3, the number of observables, $3N$, greatly exceeds the number of unknowns, $N + 9$, where 9 refers to the number of Karplus coefficients to be determined for the three types of couplings and N to the individual σ_i values. In principle, this therefore permits extraction of both the Karplus parameters, as well as the individual amplitudes of the ϕ angle fluctuations, σ_i. In practice, extracting the absolute value of the average σ_i value from such data is challenging. For example, if σ_i values were uniform, a perfect fit to eq 5 could be obtained regardless of the actual value of σ_i, which is then absorbed into the effective values of A, B, and C. Therefore, a choice for the average value of σ_i needs to be made, and extracted individual σ_i values reflect the deviation from this average value. Molecular dynamics trajectories suggest that $\sigma_i = 10°$ is a reasonable estimate for

the amplitude of ϕ angle fluctuations in well-ordered parts of a protein,[21] and we choose this average value as the reference for all residues that simultaneously meet two criteria: (1) $S^2 \geq 0.75$ on the basis of ^{15}N relaxation studies[46] and (2) none of the three J couplings deviate by more than 1.5 standard deviations from their respective Karplus curve when using the above-described parametrizations for a static structure. Residues excluded in the determination of the A, B, and C parameters by either of these two criteria are marked in the Supporting Information, Figure S5. To investigate how sensitive the results are to the assumed value of σ_i, the entire procedure is also repeated for $\sigma_i = 0°$ and for $\sigma_i = 20°$, and to evaluate how sensitive results are to the structure used, the procedure is repeated for the X-ray structure with $\sigma_i = 10°$ (Supporting Information, Table S7).

When solving the set of eqs 5, the availability of very different values of η_{ik} for any given residue, i, improves the stability of the solutions, and from this perspective $^3J_{H^N,H^\alpha}$, $^3J_{H^N,C'}$, and $^3J_{H^N,C^\beta}$ constitute an ideal set. In principle, the complementary $^3J_{C',H^\alpha}$, $^3J_{C',C'}$, and $^3J_{C',C^\beta}$ could also be measured,[23,30] but their η_{ik} values differ by ~180° relative to the set considered in this study and therefore do not contain independent information on the ϕ angle rms fluctuations, σ_i. These latter couplings are therefore not considered in this work.

Figure 5 shows how the Karplus curves for $^3J_{H^N,H^\alpha}$, $^3J_{H^N,C'}$, and $^3J_{H^N,C^\beta}$ are affected by the amplitude of ϕ angle fluctuations. Clearly, for residues such as L12, an elevated $\sigma_i = 30-35°$ results in a smaller value predicted for $^3J_{H^N,H^\alpha}$, and a better fit to the experimental data. This agrees with elevated dynamics for the amide group of this residue, previously concluded from both ^{15}N relaxation[46] and backbone RDCs.[17] Note, however, that for residues with ϕ angles close to the "nodes" in Figure 5, for which the Karplus equations are least sensitive to σ_i, little improvement in the fit is obtained. In fact, allowing the σ_i values as 47 additional, residue-specific parameters when determining the optimal Karplus parameters from eq 5 yields only very modest reductions in the goodness of the fits between experimental values and the Karplus curves. Using as a reference the single, static NMR structure (2OED), for $^3J_{H^N,H^\alpha}$ the rmsd decreases from 0.42 to 0.38 Hz, and for $^3J_{H^N,C^\beta}$ from 0.25 to 0.23 Hz, whereas for $^3J_{H^N,C'}$ it remains 0.31 Hz. Comparably small reductions are obtained when using the X-ray structure as the reference or when using an average value of $\sigma_i = 0°$ or 20° for the above-defined set of 35 most-ordered residues (Supporting Information, Table S6). In terms of standard F statistics, introduction of the 50 adjustable σ_i values in the fit is clearly not warranted, indicating that residuals in the fit to the Karplus equations are dominated by factors other than backbone dynamics. Even if all of the residuals were attributed to variations in the magnitude of the ϕ angle fluctuations, with a rmsd value of 5−6.5° (depending on the choice of the average σ_i value), these variations remain moderate and constitute an upper limit for their true variation. As expected, when a reference structure is used that demonstrates a much poorer fit to the experimental ^3J couplings, such as the 1.1-Å X-ray structure with protons added in idealized positions, attributing the increased residuals to variation in dynamics results in artificially larger ϕ angle fluctuations (Supporting Information, Table S7). This result indicates that error in the reference structure increases the spread in residue-specific σ values when

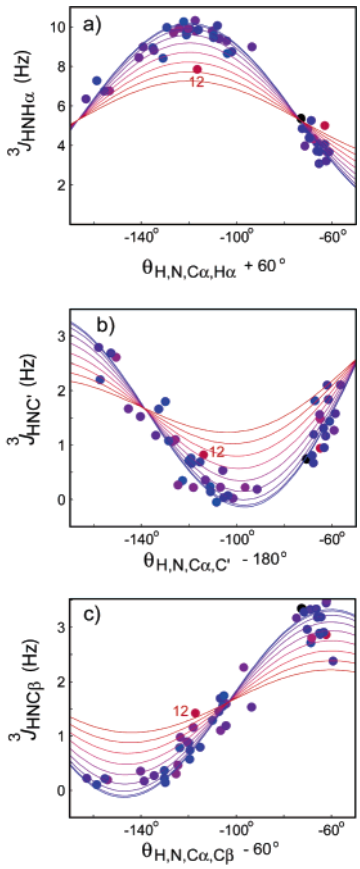

Figure 5. $^3J_{H^N,H^\alpha}$, $^3J_{H^N,C'}$, and $^3J_{H^N,C^\beta}$ versus their respective dihedral angles in the NMR structure, offset by $\pi/3$, π, and $-\pi/3$ for easy comparison of ^3J values, observed for any given residue. Karplus curves shown are for different motional amplitudes, σ, ranging from 0° (blue) to 40° (red) in steps of 5°, simultaneously optimized using eq 5 but restraining the Karplus A coefficient to the value obtained for the 35 + 3 well-ordered, well-fitting residues, for which $\sigma = 10°$ was assumed (see text). Filled circles represent the experimental ^3J values, colored according to the σ_γ motions, about the $C^\alpha_{i-1}-C^\alpha_i$ axis derived from RDC analysis.[17] Residue T25 (no σ_γ available) is shown in black.

interpreted using eq 5, and values extracted in this manner therefore must be considered as upper limits. Remarkably, the best fit to the ^3J couplings is obtained for the recent ensemble structure, calculated from the same RDCs but with additional order parameter restraints, derived from ^{15}N relaxation, and crystallographically determined temperature factors. This ensemble exhibits $\langle\sigma\rangle = 8.6 \pm 4.1°$. The improvement obtained when fitting the ^3J couplings to the ensemble NMR structure over a single-conformer NMR structure does not reflect the dynamics of the ensemble but results from an improved definition of the average dihedral angles when using the NMR restraints to derive the structure (Supporting Information, Table S6). This conclusion is supported by essentially indistinguishably good fits when using simply the ensemble-averaged dihedral angles and when fitting to the entire dynamic ensemble.

The fact that the deviations between observed ^3J values and a static Karplus curve are comparable in regions close to the "nodes" and areas where ^3J depends strongly on σ_i strongly suggests that factors other than internal dynamics dominate the differences between measured values and these empirical curves. For all three types of couplings, the residual rmsd is also considerably larger than the uncertainty in the measurements, as estimated from independent measurements using quite

different experimental schemes for each of these couplings. Therefore, likely causes may be found in the effects of hydrogen bonding, distortions in local geometry, and substituent effects. Indeed, electronegative substituents are well recognized as having a significant impact on ^3J values.[47] This latter effect has the most impact on $^3J_{H^N,C^\beta}$, where the electronegativity of the C^β-attached atoms varies with residue type. Quantum-chemical calculations confirm that residue type has a considerable effect on $^3J_{H^N,C^\beta}$, as does the side-chain χ_1 angle, which determines the orientation of the C^β substituents relative to the coupled spins (Supporting Information). The side chains for many of the residues in GB3 are dynamically disordered,[48] and correction for the side-chain "substituent" effect is therefore not readily possible. Hydrogen bonding to H^N is also calculated to have a non-negligible impact (Supporting Information), but here too, the detailed true variations in the applicable hydrogen bond lengths are not accurately known, in particular for the amides hydrogen-bonded to the solvent. Finally, bond angles at C^α are predicted to have some impact on all three types of ^3J couplings discussed in this study (Supporting Information). Although the presence of such distortions in proteins is well recognized,[49] the resolution at which protein structures are solved by crystallography and NMR is insufficient for accurate quantification at the residue-specific level.

Concluding Remarks

Our study of three-bond *J* couplings related to the backbone torsion angle ϕ in a small protein defines the limit at which such couplings can be interpreted in structural terms. Interestingly, improved agreement is observed between ^3J couplings and dihedral angles derived from an NMR structure over that obtained from the highly refined crystal structure, even when hydrogens are positioned relative to the backbone C and N atoms in the same, idealized fashion. This improvement, which occurs for all three types of *J* couplings, indicates that, although differences in the time- and ensemble-averaged backbone torsion angles, ϕ, of the structures previously determined in solution at room temperature and in the crystalline state at cryogenic temperature are very small (rmsd 3.4°), they are validated by our *J*-coupling measurements.

In conventional NMR structure determination, the number and quality of the input restraints generally are insufficient to model deviations from idealized geometry, and invariably such structures are derived using strong, artificial terms enforcing idealized values for bond lengths and angles, as well as so-called improper restraints to define planarity of aromatic groups and peptide bonds. The current structures of GB3, however, are based on an exceptionally large number of RDCs, including $^{13}C-^{13}C$, $^{13}C-^{15}N$, $^{15}N-^{1}H$, and $^{13}C-^{1}H$ interactions, measured in five different alignment media. These data were previously used to evaluate the positions of H^N and H^α atoms relative to the protein backbone and indicated small deviations from ideality.[34] The present analysis shows a remarkable improvement for all three types of *J* couplings when fitting these values to the dihedral angles defined by RDCs over those obtained when fitting these values to dihedral angles computed for hydrogens in idealized positions. Considering that, in most experimental NMR studies, lacking extensive RDC measurements in multiple media, there is insufficient information to define the deviations of the hydrogen positions from idealized positions, this result also defines the limit in using ^3J couplings in terms of deriving the backbone torsion angle ϕ in proteins.

The close agreement between quite different types of experiments for measurement of each of the $^3J_{H^N,H^\alpha}$, $^3J_{H^N,C^\beta}$, and $^3J_{H^N,C'}$ couplings excludes the possibility of substantial systematic or random errors in these values. The fact that the residual errors, when fitting these values by optimized Karplus equations to the RDC-refined protein structure, are considerably larger than the measurement uncertainties points to the presence of factors that affect ^3J couplings other than the dihedral angle. These other factors may include motion, substituent effects, geometric distortion, and hydrogen bonding. A straightforward approach to account for fluctuations in the intervening dihedral angle has previously been proposed by Bruschweiler and Case.[21] However, adding an additional term to account for motion should simultaneously improve the fits for $^3J_{H^N,H^\alpha}$, $^3J_{H^N,C^\beta}$, and $^3J_{H^N,C'}$ couplings. The absence of a statistically significant improvement indicates that motion is not the dominant reason for the residual mismatch between experimental couplings and the Karplus equations. Instead, DFT calculations suggest that these residual discrepancies are dominated by substituent effects, in particular residue type and χ_1 angle for $^3J_{H^N,C^\beta}$, small geometric distortions caused by local strain, and variations in hydrogen bonding.

Acknowledgment. We thank G. Marius Clore, Kaifeng Hu, and Dennis A. Torchia for helpful discussions, and Elena Gustchina and David Bryce for sample preparations. This work was supported by the Intramural Research Program of the NIDDK, NIH, and by the Intramural AIDS-Targeted Antiviral Program of the Office of the Director, NIH. B.V. acknowledges financial support from the Swiss National Science Foundation.

Supporting Information Available: Results from DFT calculations evaluating the effect of residue type, geometry, and hydrogen bonding on $^3J_{H^N,H^\alpha}$, $^3J_{H^N,C^\beta}$, and $^3J_{H^N,C'}$ couplings; two tables with $^3J_{H^N,H^\alpha}$, $^3J_{H^N,C^\beta}$, $^3J_{H^N,C'}$, $^1J_{C^\alpha,H^\alpha}$, $^1J_{C^\alpha,C^\beta}$, and $^1J_{C^\alpha,C'}$ values from the individual measurements; one table with Karplus parameters when using a variety of input structures; one table with motional amplitudes, σ, obtained from ^3J-coupling analysis using eq 5; three tables summarizing present and previous Karplus parameters for $^3J_{H^N,H^\alpha}$, $^3J_{H^N,C^\beta}$, and $^3J_{H^N,C'}$; one figure with Karplus curves for $^3J_{H^N,H^\alpha}$, $^3J_{H^N,C^\beta}$, and $^3J_{H^N,C'}$ and outliers marked by residue number; and a more detailed figure of the pulse sequences of Figure 1. This material is available free of charge via the Internet at http://pubs.acs.org.

JA070324O

(47) Haasnoot, C. A. G.; de Leeuw, F. A. A. M.; Altona, C. *Tetrahedron* **1980**, *36*, 2783−2792.
(48) Chou, J. J.; Case, D. A.; Bax, A. *J. Am. Chem. Soc.* **2003**, *125*, 8959−8966.
(49) Karplus, P. A. *Protein Sci.* **1996**, *5*, 1406−1420.